Solution-Mediated Selective Nanosoldering of Carbon Nanotube Junctions for Improved Device Performance

Jae-Won Do,[†,‡] Noel N. Chang,[§] David Estrada,[†,∥,⊥] Feifei Lian,[†,∥,#] Hyeongyun Cha,[▽] Xiangyun J. Duan,[†] Richard T. Haasch,[○] Eric Pop,[†,‡,∥,#] Gregory S. Girolami,[‡,§] and Joseph W. Lyding*[,†,‡]

[†]Department of Electrical and Computer Engineering, [‡]Beckman Institute for Advanced Science and Technology, [§]Department of Chemistry, [∥]Micro and Nanotechnology Laboratory, [▽]Department of Mechanical Science and Engineering, and [○]Frederick Seitz Materials Research Laboratory, University of Illinois at Urbana—Champaign, Urbana, Illinois 61801, United States, [⊥]Department of Materials Science and Engineering, Boise State University, Boise, Idaho 83725, United States, and [#]Department of Electrical Engineering, Stanford University, Stanford, California 94305, United States

ABSTRACT As-grown randomly aligned networks of carbon nanotubes (CNTs) invariably suffer from limited transport properties due to high resistance at the crossed junctions between CNTs. In this work, Joule heating of the highly resistive CNT junctions is carried out in the presence of a spin-coated layer of a suitable chemical precursor. The heating triggers thermal decomposition of the chemical precursor, tris(dibenzylideneacetone)dipalladium ($Pd_2(dba)_3$), and causes local deposition of Pd nanoparticles at the CNT junctions, thereby improving the on/off current ratio and mobility of CNT network devices by an average factor of ~6. This process can be conducted either in air or under vacuum depending on the characteristics of the precursor species. The solution-mediated nanosoldering process is simple, fast, scalable with manufacturing techniques, and extendable to the nanodeposition of a wide variety of materials.

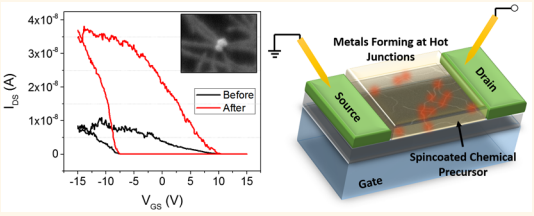

KEYWORDS: carbon nanotubes (CNT) · nanosoldering · intertube junctions · electrical resistance · thermal resistance · solution deposition

Carbon nanotubes (CNTs) have been explored extensively for a number of applications because of their exceptional electrical,[1−3] thermal,[4−6] chemical,[7,8] and mechanical[9,10] properties.[11−14] Specifically, the small dimensions and mechanical flexibility of CNTs make them potentially useful as the active channel materials in thin-film transistors (TFTs) on transparent and flexible substrates.[15−19] The performance of CNT-based TFTs is greatly enhanced by using CNTs that have been sorted according to their electrical types,[20−22] or by growing aligned CNTs[23−26] and subsequently transferring them onto suitable substrates. In addition, chemical vapor deposition (CVD) of randomly aligned CNTs can afford TFTs whose performance rivals that of organic or amorphous silicon-based devices.[27−29] Impressively, by this latter approach, mobilities of over 1000 $cm^2\ V^{-1}\ s^{-1}$ and on/off current ratios (I_{ON}/I_{OFF}) of up to 10^5 can be achieved.[29]

Although CNT networks are easy to fabricate and exhibit promising performance, they do have their share of drawbacks. In networks made from either sorted or unsorted CNTs, the carrier mobility, conductivity, and power dissipation are greatly limited by resistance at the CNT−CNT intertube junctions (CNT junctions). Theoretical and experimental studies have shown that the electrical[4,30−35] and thermal[36−40] resistances at the CNT junctions are at least an order of magnitude higher than those of individual CNTs.[30−32] As a result, even though the devices are built on an oxide, passing current through the networks causes significantly localized heating at the CNT junctions, which degrades the overall device performance and reliability.[37,40,41] Efforts have been made to lower the junction resistance by depositing nanometer scale metal particles at the CNT junctions by means of atomic force microscopy (AFM) assisted

* Address correspondence to lyding@illinois.edu.

Received for review September 30, 2014 and accepted April 6, 2015.

Published online April 06, 2015
10.1021/nn505552d

dip-pen nanolithography[42] and transmission electron microscopy (TEM) assisted electron beam (e-beam) induced deposition,[43] but these techniques require slow and serial processes to locate individual junctions. Other methods that have been proposed to decrease the sheet resistance of CNT networks include solution-based selective nucleation of fullerenes[44] and nitric acid treatment and doping of CNTs.[45] Improvements in the conductivity of CNT networks have also been achieved by constructive rehybridization of CNT sidewalls.[46−49] However, the details of the improvement in terms of electronic properties specific to transistor applications, such as mobility and I_{ON}/I_{OFF} ratio, remain unexplored.

A recent study from our group successfully demonstrated a new approach: selective deposition of metal nanosolder at the CNT junctions by a gas phase CVD process.[41] When current is passed through the CNT network, the high resistance at the CNT junctions generates nanoscale "hot spots" which trigger highly localized CVD of a metal such as Pd or HfB_2 at the CNT junctions.[41] Although this nanosoldering technique lowers junction resistance and improves the I_{ON}/I_{OFF} ratio, this CVD process limits the composition of the nanosolder to those materials for which there is a volatile CVD precursor with an onset temperature for deposition which is not too high.

In this study, we describe a solution-based alternative to this CVD method which is also able to deposit nanometer scale metal selectively at the CNT junctions. The new process involves spin-coating a chemical precursor from a volatile solvent to layer a thin film of the precursor on top of the CNT network. Subsequent passage of current through the network causes localized heating at the CNT junctions and induces selective thermal decomposition of the precursor. After the nanometer scale metal particles are deposited on the CNT junctions, the thermolysis byproducts and unreacted precursor are rinsed away. By using this non-CVD technique, we have been able to deposit nanometer scale Pd particles selectively at CNT junctions and improve the I_{ON}/I_{OFF} ratio and mobility of CNT networks by an average factor of ~6. This solution-mediated technique is simple, fast, scalable with manufacturing techniques, and easily extendable to the deposition of other materials.

RESULTS AND DISCUSSION

We chose to deposit Pd onto the CNT junctions because Pd is known to form ohmic contacts to p-type CNT devices operating in air; this behavior is a consequence of the high work function of Pd and its favorable interaction with CNT sidewalls.[41,50−53] The Pd compound $Pd_2(dba)_3$ (where dba = dibenzoylacetone), which contains a zerovalent Pd metal center, is widely used as a Pd source in cross-coupling and alkene hydrosilylation reactions.[54,55] It is soluble in common

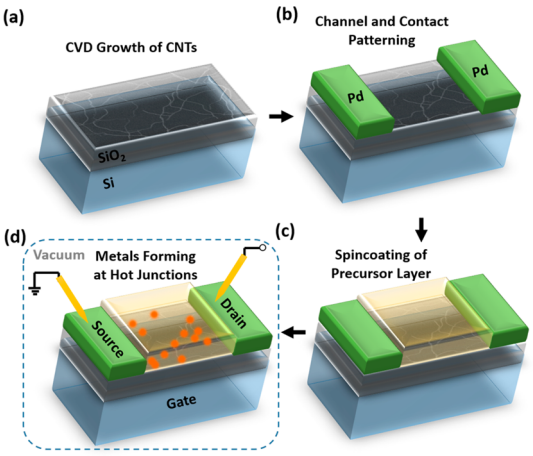

Figure 1. Schematic diagrams of (a) carbon nanotube (CNT) network growth on a SiO_2/Si substrate by chemical vapor deposition (CVD), (b) device fabrication using standard photolithography and e-beam evaporation for channel and contact patterning with Ti/Pd (0.5/40 nm) electrodes, (c) solution-mediated application of the $Pd_2(dba)_3$ precursor onto CNT networks by spin-coating, and (d) selective Pd deposition triggered by resistive heating at CNT junctions under device operation in vacuum probe station.

organic solvents and can be handled in air, making it well suited for spin-coating applications.[56]

First it is necessary to determine whether the thermal decomposition of $Pd_2(dba)_3$ leads to elemental Pd. We find by thermogravimetric analysis (TGA) that the thermal decomposition of $Pd_2(dba)_3$ begins at ~180 °C. In a preliminary study detailed in the Supporting Information, $Pd_2(dba)_3$ was dissolved in dichloromethane and drop-cast onto three SiO_2/Si substrates. After the solvent had evaporated, one sample was stored in air at room temperature, one sample was heated in vacuum to 250 °C, and one sample was heated in air to 250 °C for 90 min. Each sample was rinsed with dichloromethane to remove the byproducts and the excess reactants. The samples were then examined by X-ray photoelectron spectroscopy (XPS) and energy dispersive X-ray spectroscopy (EDS). The sample that had been stored in air at room temperature had very little Pd; it contained only traces of PdO and PdO_2, which are likely present as impurities in the commercial reagent.[56] Thermolysis of $Pd_2(dba)_3$ in air gives exclusively PdO, but thermolysis under vacuum predominantly yields metallic Pd. We employed heating in vacuum for all our subsequent studies.

Selective metal deposition of Pd onto CNT network devices supported on SiO_2/Si substrates was carried out as shown in Figure 1. As detailed in the Methods section, the CNTs were grown by ferritin-catalyzed CVD from methane gas on a thermally grown 300 nm SiO_2 layer atop a highly doped Si substrate, which acts as a global back-gate. Then, standard photolithography and e-beam evaporation were used to define the channel and the metal electrodes, which consisted of 0.5 nm Ti as an adhesion layer and 40 nm Pd.

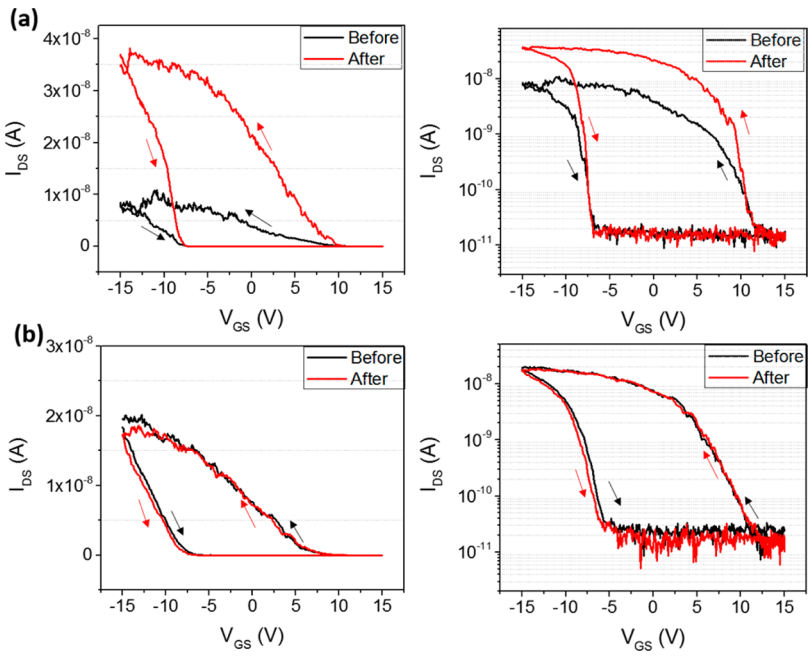

Figure 2. Transfer characteristics of (a) a CNT network device before and after Pd deposition in (left) linear and (right) log scales with V_{DS} = 1 V. The arrows indicate V_{GS} sweep direction and (b) a control CNT network device before precursor application and after rinsing away the precursor and drying in (left) linear and (right) log scales with V_{DS} = 1 V, showing no change in the device performance. Channel length and width are L = 150 μm and W = 50 μm, respectively for both devices.

Spin-coating from chloroform was used to deposit a ~180 nm $Pd_2(dba)_3$ film. The $Pd_2(dba)_3$ coated device was loaded into a vacuum-capable probe station, which was evacuated to a base pressure of $\sim 10^{-5}$ Torr. *In-situ* metal probes were used to contact individual devices and apply various voltages over specific time periods to locally heat the CNT junctions and induce selective thermal decomposition of $Pd_2(dba)_3$. After the deposition, the samples were removed from the vacuum probe station, rinsed thoroughly with clean solvent, and dried.

Figure 2a shows the transfer characteristic curves (V_{GS} = −15 to 15 V and V_{DS} = 1 V) of a CNT network device whose channel length and width are L = 150 μm and W = 50 μm, respectively, before and after Pd deposition. To deposit Pd at the CNT junctions, V_{DS} was applied for ~1.5 s periods first at 10 V and then at increasingly larger biases (up to a maximum of 150 V). V_{GS} was set to either −30 or 30 V depending on whether the device exhibits p-type or n-type behavior; as current is passed and the associated heating in vacuum removes oxygen from the device, the metal−CNT interface is altered and the device slowly converts from p-type to n-type.[41,57−59] V_{GS} was chosen such that both metallic and semiconducting CNTs are "turned on" and carry the highest current possible. This protocol was carefully followed until there was no longer any noticeable change in the transfer characteristics in order to avoid overheating of the CNT network, which could cause overdeposition of Pd and electrically short the device. The results indicate that I_{ON} was improved by a factor of ~4.4, whereas I_{OFF} remained essentially the same, in agreement with our previous results using gas-phase CVD methods.[41] To calculate I_{ON}/I_{OFF} ratios, we used the threshold voltage (V_T) found by the linear extrapolation method from peak transconductance ($g_m = (dI_D/dV_{GS})_{max}$), I_{ON} at a constant V_{GS} overdrive from the forward sweep ($V_{GS} - V_{T,FWD} = -10$ V), and I_{OFF} as the minimum I_{DS} from the same transfer curve.[27]

Deposition of Pd also improves the field-effect mobility of the devices, μ_{FE}, by a factor of ~3.9 from 0.97 $cm^2/(V\,s)$ to 3.78 $cm^2/(V\,s)$, as determined from the relation[27] $\mu_{FE} = g_m L/(WC_{OX}V_{DS})$, where C_{OX} = 1.04 × 10^{-8} F/cm^2 is the gate capacitance per unit area calculated from the parallel plate model of the SiO_2. We note that the parallel plate model overestimates the gate capacitance, and thus underestimates μ_{FE} for low-density CNT networks because only a portion of the gate oxide is covered by CNTs.[28,60,61] Image analysis reveals that the fill factor of our networks is ~0.024; that is, approximately 2.4% of the device channel is covered by CNTs.[40] However, this effect does not interfere with our analysis of the relative improvement in μ_{FE}, which is measured by a comparison of values before and after metal deposition.

Figure 2b shows the transfer characteristics in a control experiment in which the $Pd_2(dba)_3$ precursor was spin-coated, the coated device was exposed to vacuum, and the device was rinsed with solvent *without* performing the nanosoldering step, that is, without passing any current through the CNT network. There is essentially no improvement in the transfer characteristics after this treatment. A related control experiment was performed in which the spin-coating

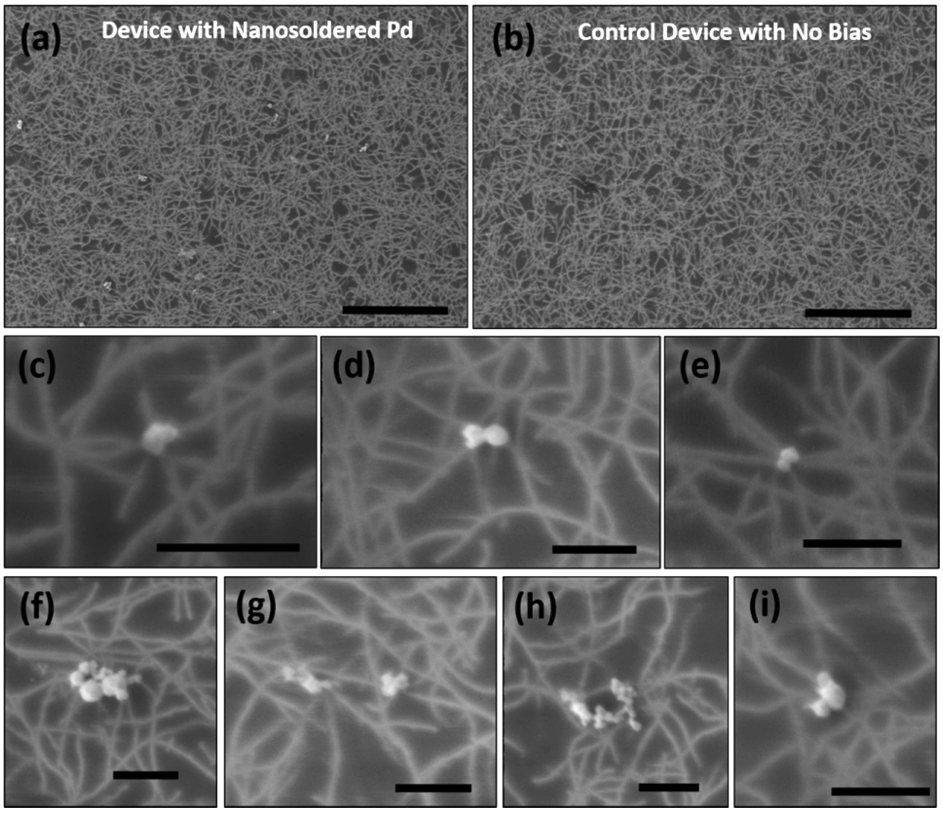

Figure 3. (a) A scanning electron microscope (SEM) image of a CNT network after Pd deposition. Scale bar is 5 μm. (b) An SEM image of a control device onto which precursor was applied without any current flow, showing no noticeable Pd particles. Scale bar is 5 μm. (c–i) Magnified SEM images of CNT network showing CNT junctions nanosoldered with Pd particles. The scale bar is 1 μm.

was carried out with a pure chloroform solution, the device was subjected to Joule heating under vacuum and then rinsed. No significant improvement was observed under these conditions either. For the six devices on which we deposited Pd *via* our solution-mediated process, the average improvements in the I_{ON}/I_{OFF} ratio and mobility values were ~6.3 and ~6.0, respectively. For five control devices in which the Pd precursor or the heating step was omitted, there was no significant change in the I_{ON}/I_{OFF} ratio and μ_{FE} values (see Supporting Information).

Some hysteresis is apparent in the transfer characteristics of our devices, as is commonly observed for unencapsulated CNT network devices on back-gated SiO_2/Si substrates.[62−64] The hysteresis can arise from several factors, including charge injection into the dielectric substrate, charge trapping by surrounding water molecules, or electrochemical reaction of water and oxygen redox couples.[65−70] The threshold voltage hysteresis ($V_{T,FWD} - V_{T,REV}$) of nanosoldered devices and control devices not nanosoldered with the Pd precursor are 0.097 ± 0.50 V and −0.13 ± 0.51 V, respectively, which suggests that the solution-mediated deposition process does not introduce significant new trap states near the CNT/SiO_2 interface.[65]

Figure 3a shows a scanning electron microscope (SEM) image of a CNT network after Pd deposition, and Figure 3b shows a control device, in which the precursor was applied onto a CNT network but no current was passed showing no noticeable signs of metal particles or residues. Figures 3 panels c–i show magnified SEM images of the areas where Pd was selectively deposited at the CNT junctions, that is, at hot spots under device operation. According to the AFM images shown in the Supporting Information, the Pd particles are ~30–130 nm in height. It is highly likely that there exist other junctions at which some Pd deposition had occurred, but the amount is too small to be visible by means of SEM or AFM.

Because the junction resistance depends on many factors, including the separation distance, overlap area, and the electrical types of CNTs involved in the intertube junctions,[34−36] some CNT junctions may undergo Pd deposition at lower current (corresponding to lower V_{DS}) than other CNT junctions. Because the deposited metal lowers the junction resistance (by increasing the area available for carrier flow and reducing energy barrier), more current can now pass through the same CNT junctions. When V_{DS} is increased even more to deposit Pd elsewhere, already-deposited CNT junctions may still get hot enough to cause thermal decomposition of leftover $Pd_2(dba)_3$ precursor, which may result in varying heights of deposited Pd particles.

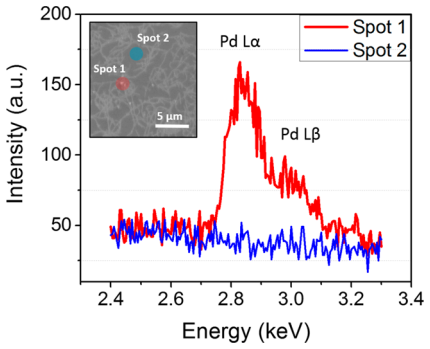

Figure 4. Energy dispersive X-ray spectroscopy (EDS) spectrum from a CNT network after Pd deposition. The red curve is collected from spot 1 and the blue curve is collected from spot 2 in the inset SEM image, corresponding to bright particles at carbon nanotube junctions and on the bare SiO_2 surface, respectively. The EDS data indicate that the deposited material is indeed Pd and that the obtained spectrum is not simply from impurities or residues of the precursor solution.

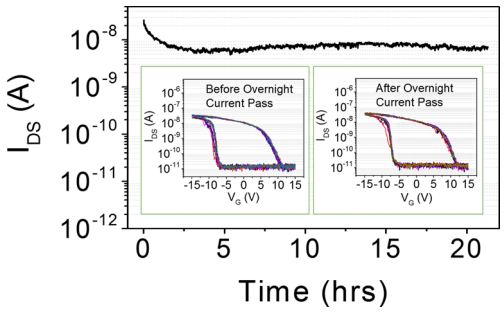

Figure 5. Time-dependence measurement of a CNT network device after Pd nanosoldering with V_{DS} = 1 V and V_{GS} = −15 V. Channel length and width are L = 150 μm and W = 50 μm, respectively. After an initial current drop for about 1.2 h, the current stays stable for the remaining 20 h of the test. The inset plots show consistent transfer characteristic curves (left) before and (right) after the 21 h current pass treatment. Each plot is composed of 10 transfer curves measured consecutively.

To confirm that deposited particles are indeed Pd, we performed EDS measurements on a Pd-nanosoldered device. The red curve in Figure 4 shows the EDS spectrum obtained from a bright particle located at a CNT junction (Spot 1 in the inset SEM image), whereas the blue curve shows the EDS spectrum obtained from the bare SiO_2 surface (Spot 2). The data clearly suggest that Pd has been deposited selectively at the CNT junctions.

Figure 5 shows the results of an air stability test performed on the Pd-nanosoldered device from Figure 2a. After 10 transfer characteristic curves were initially measured, current was passed through the device in air for 21 h with V_{DS} = 1 V and V_{GS} = −15 V. After this time, an additional 10 transfer characteristic curves were measured. The stability test shows that the current I_{DS} decreases over the first 1.2 h by about a factor of 3. Most likely, this decrease is due to the increasing adsorption of water molecules, which either act as electron donors for the p-type CNTs or the trap charges to create a positive electric potential that reduces the effective negative V_{GS}.[69,71−74] After the initial decrease, the current stayed relatively stable for the remaining 20 h of the test. The stable current during the device operation in Figure 5 and consistent transfer curves before and after the 21 h current pass indicate that our technique does not cause any stability issues related to possible electromigration or oxidation of deposited Pd.

CONCLUSION

We developed a new technique to deposit nanoscale metal selectively at CNT junctions; this bottom-up nanosoldering method lowers the resistivity of the junctions in CNT network devices. The resistive CNT junctions were locally heated by passing current across the device, which promotes thermal decomposition of a spin-coated chemical precursor and deposition of metal (here, Pd) at the heated CNT junctions, improving the overall transport characteristics of the device. This solution-mediated application process does not require volatile precursors, and is simple, fast, and scalable with manufacturing techniques. This process can easily be generalized to deposit other nanomaterials onto CNT network devices in a selective fashion.

METHODS

CNT Growth and Device Fabrication. CNTs were grown by CVD with the assistance of a ferritin catalyst (Sigma-Aldrich), which was diluted in deionized water and spin-coated on thermally grown 300 nm SiO_2 films on a highly boron-doped silicon substrate (resistivity 0.05 Ω·cm). Before CNT growth, the catalyst was oxidized by heating the wafer in air to 900 °C. After the wafer had been cooled to room temperature in air, the catalyst was reduced by heating it to 900 °C under H_2. Then, the randomly aligned CNT networks were grown from a mixture of CH_4 and H_2 at 900 °C for 15 min. The CNT networks were patterned by standard photolithography and O_2 plasma etching. For electrodes, 40 nm of Pd was evaporated onto a 0.5 nm Ti layer used to improve adhesion to the SiO_2 film, and patterned by lift-off. Image analysis with Gwyddion reveals that the fill factor of our networks is 0.024; that is, that approximately 2.4% of the device channel is covered by CNTs.[40]

$Pd_2(dba)_3$ and Sample Preparation. $Pd_2(dba)_3$ was purchased from Aldrich and purified by methods described elsewhere.[56] About 12.0 mg of $Pd_2(dba)_3$ was dissolved in 1.0 mL of chloroform, and the solution was spin-coated at 1500 rpm for 30 s onto the CNT network devices on SiO_2/Si substrates. After the chloroform had evaporated in air, the sample was loaded into a vacuum probe station connected to a turbo pump that kept the pressure ~10^{-5} Torr.

Measurements and Characterizations. All in-air and vacuum DC electrical measurements were performed using a Keithley 4200-SCS semiconductor analyzer and a Janis variable temperature probe station. Transfer characteristics were measured in air for each device before metal deposition. After Pd particles were deposited in vacuum and the byproducts and excess precursor were removed by rinsing the substrates with clean solvents, the transfer characteristic curves were remeasured in air. To calculate the I_{ON}/I_{OFF} ratios, we used I_{ON} at a constant V_{GS} overdrive

from the forward sweep ($V_{GS} - V_{T,FWD} = -10$ V) and used I_{OFF} as the minimum I_{DS} from the same transfer curve.[27] Note that for devices with I_{OFF} lower than the measurement limit, we used I_{OFF} by averaging currents in the fluctuating region in the off state below V_T (see Supporting Information). SEM images were collected on a Philips XL30 ESEM-FEG instrument at an operating voltage of 1 kV. EDS analysis was performed using a FEI XL-30 SEM with field emission gun (FEG) source. AFM images were collected using a Bruker Dimension IV AFM in tapping mode. The scan size was 7 μm $\times$ 7 μm with a scan rate of 0.5 Hz. The resolution was 1024 $\times$ 1024 pixels, and the drive amplitude and set point were carefully monitored to ensure good tracking of the surface.

Conflict of Interest: The authors declare no competing financial interest.

Supporting Information Available: Details of Pd precursor study including air sensitivity test, TGA, XPS, and EDS analyses, control experiments, and additional data analysis. This material is available free of charge *via* the Internet at http://pubs.acs.org.

Acknowledgment. This work was supported by the National Science Foundation (NSF) under Grants CHE 13-62931 (J.W.L. and G.S.G.) and ECCS CAREER 09-43323 (E.P.), the Office of Naval Research Grant N00014-13-1-0300 (J.W.L.), and the Army Research Office grant W911NF-11-1-0066 (E.P.). D.E. acknowledges support from the National Defense Science and Engineering Graduate Fellowship and the NSF Graduate Fellowship programs. This work was carried out in part in the Frederick Seitz Materials Research Laboratory Central Research Facilities, University of Illinois.

REFERENCES AND NOTES

1. Cao, Q.; Han, S.; Tulevski, G. S.; Zhu, Y.; Lu, D. D.; Haensch, W. Arrays of Single-Walled Carbon Nanotubes with Full Surface Coverage for High-Performance Electronics. *Nat. Nanotechnol.* **2013**, *8*, 180–186.
2. Appenzeller, J. Carbon Nanotubes for High-Performance Electronics; Progress and Prospect. *Proc. IEEE* **2008**, *96*, 201–211.
3. Tans, S. J.; Verschueren, A. R. M.; Dekker, C. Room-Temperature Transistor Based on a Single Carbon Nanotube. *Nature* **1998**, *393*, 49–52.
4. Behnam, A.; Sangwan, V. K.; Zhong, X.; Lian, F.; Estrada, D.; Jariwala, D.; Hoag, A. J.; Lauhon, L. J.; Marks, T. J.; Hersam, M. C.; *et al*. High-Field Transport and Thermal Reliability of Sorted Carbon Nanotube Network Devices. *ACS Nano* **2013**, *7*, 482–490.
5. Panzer, M. A.; Zhang, G.; Mann, D.; Hu, X.; Pop, E.; Dai, H.; Goodson, K. E. Thermal Properties of Metal-Coated Vertically Aligned Single-Wall Nanotube Arrays. *J. Heat Transfer* **2008**, *130*, 52401.
6. Han, Z.; Fina, A. Thermal Conductivity of Carbon Nanotubes and Their Polymer Nanocomposites: A Review. *Prog. Polym. Sci.* **2011**, *36*, 914–944.
7. Bondavalli, P.; Legagneux, P.; Pribat, D. Carbon Nanotubes Based Transistors as Gas Sensors: State of the Art and Critical Review. *Sens. Actuators, B* **2009**, *140*, 304–318.
8. Maehashi, K.; Matsumoto, K. Label-Free Electrical Detection Using Carbon Nanotube-Based Biosensors. *Sensors* **2009**, *9*, 5368–5378.
9. Zhang, R.; Wen, Q.; Qian, W.; Su, D. S.; Zhang, Q.; Wei, F. Superstrong Ultralong Carbon Nanotubes for Mechanical Energy Storage. *Adv. Mater.* **2011**, *23*, 3387–3391.
10. Di, J.; Hu, D.; Chen, H.; Yong, Z.; Chen, M.; Feng, Z.; Zhu, Y.; Li, Q. Ultrastrong, Foldable, and Highly Conductive Carbon Nanotube Film. *ACS Nano* **2012**, *6*, 5457–5464.
11. Baughman, R. H.; Zakhidov, A. A.; de Heer, W. A. Carbon Nanotubes—The Route toward Applications. *Science* **2002**, *297*, 787–792.
12. De Volder, M. F. L.; Tawfick, S. H.; Baughman, R. H.; Hart A. J. Carbon Nanotubes: Present and Future Commercial Applications. *Science* **2013**, *339*, 535–539.
13. Avouris, P.; Freitag, M.; Perebeinos, V. Carbon-Nanotube Photonics and Optoelectronics. *Nat. Photonics* **2008**, *2*, 341–350.
14. Wang, C.; Takei, K.; Takahashi, T.; Javey, A. Carbon Nanotube Electronics—Moving Forward. *Chem. Soc. Rev.* **2013**, *42*, 2592–2609.
15. Zhang, D.; Ryu, K.; Liu, X.; Polikarpov, E.; Ly, J.; Tompson, M. E.; Zhou, C. Transparent, Conductive, and Flexible Carbon Nanotube Films and Their Application in Organic Light-Emitting Diodes. *Nano Lett.* **2006**, *6*, 1880–1886.
16. Ha, M.; Xia, Y.; Green, A. A.; Zhang, W.; Renn, M. J.; Kim, C. H.; Hersam, M. C.; Frisbie, C. D. Printed, Sub-3V Digital Circuits on Plastic from Aqueous Carbon Nanotube Inks. *ACS Nano* **2010**, *4*, 4388–4395.
17. Takahashi, T.; Yu, Z.; Chen, K.; Kiriya, D.; Wang, C.; Takei, K.; Shiraki, H.; Chen, T.; Ma, B.; Javey, A. Carbon Nanotube Active-Matrix Backplanes for Mechanically Flexible Visible Light and X-ray Imagers. *Nano Lett.* **2013**, *13*, 5425–5430.
18. Cho, D.-Y.; Eun, K.; Choa, S.-H.; Kim, H.-K. Highly Flexible and Stretchable Carbon Nanotube Network Electrodes Prepared by Simple Brush Painting for Cost-Effective Flexible Organic Solar Cells. *Carbon* **2014**, *66*, 530–538.
19. Park, S.; Vosguerichian, M.; Bao, Z. A Review of Fabrication and Applications of Carbon Nanotube Film-Based Flexible Electronics. *Nanoscale* **2013**, *5*, 1727–1752.
20. Hersam, M. C. Progress Towards Monodisperse Single-Walled Carbon Nanotubes. *Nat. Nanotechnol.* **2008**, *3*, 387–394.
21. Arnold, M. S.; Green, A. A.; Hulvat, J. F.; Stupp, S. I.; Hersam, M. C. Sorting Carbon Nanotubes by Electronic Structure Using Density Differentiation. *Nat. Nanotechnol.* **2006**, *1*, 60–65.
22. Brady, G. J.; Joo, Y.; Singha Roy, S.; Gopalan, P.; Arnold, M. S. High Performance Transistors *via* Aligned Polyfluorene-Sorted Carbon Nanotubes. *Appl. Phys. Lett.* **2014**, *104*, 83107.
23. Kang, S. J.; Kocabas, C.; Ozel, T.; Shim, M.; Pimparkar, N.; Alam, M. A.; Rotkin, S. V.; Rogers, J. A. High-Performance Electronics Using Dense, Perfectly Aligned Arrays of Single-Walled Carbon Nanotubes. *Nat. Nanotechnol.* **2007**, *2*, 230–236.
24. Kocabas, C.; Hur, S.-H.; Gaur, A.; Meitl, M. A. A.; Shim, M.; Rogers, J. A. A. Guided Growth of Large-Scale, Horizontally Aligned Arrays of Single-Walled Carbon Nanotubes and Their Use in Thin-Film Transistors. *Small* **2005**, *1*, 1010–1017.
25. Engel, M.; Small, J. P.; Steiner, M.; Freitag, M.; Green, A. A.; Hersam, M. C.; Avouris, P. Thin Film Nanotube Transistors Based on Self-Assembled, Aligned, Semiconducting Carbon Nanotube Arrays. *ACS Nano* **2008**, *2*, 2445–2452.
26. Xiao, J.; Dunham, S.; Liu, P.; Zhang, Y.; Kocabas, C.; Moh, L.; Huang, Y.; Hwang, K.-C.; Lu, C.; Huang, W.; *et al*. Alignment Controlled Growth of Single-Walled Carbon Nanotubes on Quartz Substrates. *Nano Lett.* **2009**, *9*, 4311–4319.
27. Timmermans, M. Y.; Estrada, D.; Nasibulin, A. G.; Wood, J. D.; Behnam, A.; Sun, D.; Ohno, Y.; Lyding, J. W.; Hassanien, A.; Pop, E.; *et al*. Effect of Carbon Nanotube Network Morphology on Thin Film Transistor Performance. *Nano Res.* **2012**, *5*, 307–319.
28. Cao, Q.; Kim, H.; Pimparkar, N.; Kulkarni, J. P.; Wang, C.; Shim, M.; Roy, K.; Alam, M. A.; Rogers, J. A. Medium-Scale Carbon Nanotube Thin-Film Integrated Circuits on Flexible Plastic Substrates. *Nature* **2008**, *454*, 495–500.
29. Sun, D.-M.; Timmermans, M. Y.; Kaskela, A.; Nasibulin, A. G.; Kishimoto, S.; Mizutani, T.; Kauppinen, E. I.; Ohno, Y. Mouldable All-Carbon Integrated Circuits. *Nat. Commun.* **2013**, *4*, 2302.
30. Hu, L.; Hecht, D. S.; Grüner, G. Percolation in Transparent and Conducting Carbon Nanotube Networks. *Nano Lett.* **2004**, *4*, 2513–2517.
31. Nirmalraj, P. N.; Lyons, P. E.; De, S.; Coleman, J. N.; Boland, J. J. Electrical Connectivity in Single-Walled Carbon Nanotube Networks. *Nano Lett.* **2009**, *9*, 3890–3895.
32. Stadermann, M.; Papadakis, S.; Falvo, M.; Novak, J.; Snow, E.; Fu, Q.; Liu, J.; Fridman, Y.; Boland, J. Superfine, R.; *et al*. Nanoscale Study of Conduction through Carbon Nanotube Networks. *Phys. Rev. B* **2004**, *69*, 201402.
33. Kumar, S.; Alam, M. A.; Murthy, J. Y. Effect of Percolation on Thermal Transport in Nanotube Composites. *Appl. Phys. Lett.* **2007**, *90*, 104105.

34. Kyrylyuk, A. V.; Hermant, M. C.; Schilling, T.; Klumperman, B.; Koning, C. E.; van der Schoot, P. Controlling Electrical Percolation in Multicomponent Carbon Nanotube Dispersions. *Nat. Nanotechnol.* **2011**, *6*, 364–369.
35. Fuhrer, M. S.; Nygard, J.; Shih, L.; Forero, M.; Yoon, Y. G.; Mazzoni, M. S. C.; Choi, H. J.; Ihm, J.; Louie, S. G.; Zettl, A.; *et al*. Crossed Nanotube Junctions. *Science* **2000**, *288*, 494–497.
36. Alam, M. A. A.; Pimparkar, N.; Kumar, S.; Murthy, J. Theory of Nanocomposite Network Transistors for Macroelectronics Applications. *MRS Bull.* **2006**, *31*, 466–470.
37. Zhong, H.; Lukes, J. Interfacial Thermal Resistance between Carbon Nanotubes: Molecular Dynamics Simulations and Analytical Thermal Modeling. *Phys. Rev. B* **2006**, *74*, 125403.
38. Prasher, R.; Hu, X.; Chalopin, Y.; Mingo, N.; Lofgreen, K.; Volz, S.; Cleri, F.; Keblinski, P. Turning Carbon Nanotubes from Exceptional Heat Conductors into Insulators. *Phys. Rev. Lett.* **2009**, *102*, 105901.
39. Yang, J.; Waltermire, S.; Chen, Y.; Zinn, A. A.; Xu, T. T.; Li, D. Contact Thermal Resistance between Individual Multiwall Carbon Nanotubes. *Appl. Phys. Lett.* **2010**, *96*, 023109.
40. Estrada, D.; Pop, E. Imaging Dissipation and Hot Spots in Carbon Nanotube Network Transistors. *Appl. Phys. Lett.* **2011**, *98*, 073102.
41. Do, J.-W.; Estrada, D.; Xie, X.; Chang, N. N.; Mallek, J.; Girolami, G. S.; Rogers, J. A.; Pop, E.; Lyding, J. W. Nanosoldering Carbon Nanotube Junctions by Local Chemical Vapor Deposition for Improved Device Performance. *Nano Lett.* **2013**, *13*, 5844–5850.
42. Shen, G.; Lu, Y.; Shen, L.; Zhang, Y.; Guo, S. Nondestructively Creating Nanojunctions by Combined-Dynamic-Mode Dip-Pen Nanolithography. *ChemPhysChem* **2009**, *10*, 2226–2229.
43. Wang, M. S.; Wang, J. Y.; Chen, Q.; Peng, L.-M. Fabrication and Electrical and Mechanical Properties of Carbon Nanotube Interconnections. *Adv. Funct. Mater.* **2005**, *15*, 1825–1831.
44. Virkar, A. *Investigating the Nucleation, Growth, and Energy Levels of Organic Semiconductors for High Performance Plastic Electronics*; Springer: New York, 2012; pp 115−128.
45. Znidarsic, A.; Kaskela, A.; Laiho, P.; Gaberscek, M.; Ohno, Y.; Nasibulin, A. G.; Kauppinen, E. E. I.; Hassanien, A. Spatially Resolved Transport Properties of Pristine and Doped Single-Walled Carbon Nanotube Networks. *J. Phys. Chem. C* **2013**, *117*, 13324–13330.
46. Wang, F.; Itkis, M. E.; Bekyarova, E.; Sarkar, S.; Tian, X.; Haddon, R. C. Solid-State Bis-Hexahapto-Metal Complexation of Single-Walled Carbon Nanotubes. *J. Phys. Org. Chem.* **2012**, *25*, 607–610.
47. Wang, F.; Itkis, M. E.; Bekyarova, E. B.; Tian, X.; Sarkar, S.; Pekker, A.; Kalinina, I.; Moser, M. L.; Haddon, R. C. Effect of First Row Transition Metals on the Conductivity of Semiconducting Single-Walled Carbon Nanotube Networks. *Appl. Phys. Lett.* **2012**, *100*, 223111.
48. Tian, X.; Moser, M. L.; Pekker, A.; Sarkar, S.; Ramirez, J.; Bekyarova, E.; Itkis, M. E.; Haddon, R. C. Effect of Atomic Interconnects on Percolation in Single-Walled Carbon Nanotube Thin Film Networks. *Nano Lett.* **2014**, *14*, 3930–3937.
49. Bekyarova, E.; Sarkar, S.; Wang, F.; Itkis, M. E.; Kalinina, I.; Tian, X.; Haddon, R. C. Effect of Covalent Chemistry on the Electronic Structure and Properties of Carbon Nanotubes and Graphene. *Acc. Chem. Res.* **2013**, *46*, 65–76.
50. Gu, D.; Dey, S. K.; Majhi, P. Effective Work Function of Pt, Pd, and Re on Atomic Layer Deposited HfO_2. *Appl. Phys. Lett.* **2006**, *89*, 082907.
51. Skriver, H.; Rosengaard, N. Surface Energy and Work Function of Elemental Metals. *Phys. Rev. B* **1992**, *46*, 7157–7168.
52. Zhang, Y.; Franklin, N. W.; Chen, R. J.; Dai, H. Metal Coating on Suspended Carbon Nanotubes and Its Implication to Metal−Tube Interaction. *Chem. Phys. Lett.* **2000**, *331*, 35–41.
53. Zhang, Y.; Dai, H. Formation of Metal Nanowires on Suspended Single-Walled Carbon Nanotubes. *Appl. Phys. Lett.* **2000**, *77*, 3015–3017.
54. Old, D. W.; Wolfe, J. P.; Buchwald, S. L. A Highly Active Catalyst for Palladium-Catalyzed Cross-Coupling Reactions: Room-Temperature Suzuki Couplings and Amination of Unactivated Aryl Chlorides. *J. Am. Chem. Soc.* **1998**, *120*, 9722–9723.
55. Sumida, Y.; Kato, T.; Yoshida, S.; Hosoya, T. Palladium-Catalyzed Regio- and Stereoselective Hydrosilylation of Electron-Deficient Alkynes. *Org. Lett.* **2012**, *14*, 1552–1555.
56. Zalesskiy, S. S.; Ananikov, V. P. $Pd_2(dba)_3$ as a Precursor of Soluble Metal Complexes and Nanoparticles: Determination of Palladium Active Species for Catalysis and Synthesis. *Organometallics* **2012**, *31*, 2302–2309.
57. Derycke, V.; Martel, R.; Appenzeller, J.; Avouris, P. Controlling Doping and Carrier Injection in Carbon Nanotube Transistors. *Appl. Phys. Lett.* **2002**, *80*, 2773.
58. Huang, W.; Zhai, R.; Bao, X. Investigation of Oxygen Adsorption on Pd (100) with Defects. *Appl. Surf. Sci.* **2000**, *158*, 287–291.
59. Cui, X.; Freitag, M.; Martel, R.; Brus, L.; Avouris, P. Controlling Energy-Level Alignments at Carbon Nanotube/Au Contacts. *Nano Lett.* **2003**, *3*, 783–787.
60. Cao, Q.; Xia, M.; Kocabas, C.; Shim, M.; Rogers, J. A.; Rotkin, S. V. Gate Capacitance Coupling of Singled-Walled Carbon Nanotube Thin-Film Transistors. *Appl. Phys. Lett.* **2007**, *90*, 023516.
61. Wang, C.; Chien, J.-C.; Takei, K.; Takahashi, T.; Nah, J.; Niknejad, A. M.; Javey, A. Extremely Bendable, High-Performance Integrated Circuits Using Semiconducting Carbon Nanotube Networks for Digital, Analog, and Radio-Frequency Applications. *Nano Lett.* **2012**, *12*, 1527–1533.
62. Jin, S. H.; Islam, A. E.; Kim, T.; Kim, J.; Alam, M. A.; Rogers, J. A. Sources of Hysteresis in Carbon Nanotube Field-Effect Transistors and Their Elimination *via* Methylsiloxane Encapsulants and Optimized Growth Procedures. *Adv. Funct. Mater.* **2012**, *22*, 2276–2284.
63. Kim, S. K.; Xuan, Y.; Ye, P. D.; Mohammadi, S.; Back, J. H.; Shim, M. Atomic Layer Deposited Al_2O_3 for Gate Dielectric and Passivation Layer of Single-Walled Carbon Nanotube Transistors. *Appl. Phys. Lett.* **2007**, *90*, 163108.
64. Helbling, T.; Hierold, C.; Roman, C.; Durrer, L.; Mattmann, M.; Bright, V. M. Long Term Investigations of Carbon Nanotube Transistors Encapsulated by Atomic-Layer-Deposited Al_2O_3 for Sensor Applications. *Nanotechnology* **2009**, *20*, 434010.
65. Estrada, D.; Dutta, S.; Liao, A.; Pop, E. Reduction of Hysteresis for Carbon Nanotube Mobility Measurements Using Pulsed Characterization. *Nanotechnology* **2010**, *21*, 85702.
66. Lee, J. S.; Ryu, S.; Yoo, K.; Choi, I. S.; Yun, W. S.; Kim, J. Origin of Gate Hysteresis in Carbon Nanotube Field-Effect Transistors. *J. Phys. Chem. C* **2007**, *111*, 12504–12507.
67. Ong, H. G.; Cheah, J. W.; Zou, X.; Li, B.; Cao, X. H.; Tantang, H.; Li, L.-J.; Zhang, H.; Han, G. C.; Wang, J. Origin of Hysteresis in the Transfer Characteristics of Carbon Nanotube Field-Effect Transistor. *J. Phys. D Appl. Phys.* **2011**, *44*, 285301.
68. Pascal-Levy, Y.; Shifman, E.; Pal-Chowdhury, M.; Kalifa, I.; Rabkin, T.; Shtempluck, O.; Razin, A.; Kochetkov, V.; Yaish, Y. E. Water-Assisted Mobile Charge Induced Screening and Origin of Hysteresis in Carbon Nanotube Field-Effect Transistors. *Phys. Rev. B* **2012**, *86*, 115444.
69. Kim, W.; Javey, A.; Vermesh, O.; Wang, Q.; Li, Y.; Dai, H. Hysteresis Caused by Water Molecules in Carbon Nanotube Field-Effect Transistors. *Nano Lett.* **2003**, *3*, 193–198.
70. Aguirre, C. M.; Levesque, P. L.; Paillet, M.; Lapointe, F.; St-Antoine, B. C.; Desjardins, P.; Martel, R. The Role of the Oxygen/Water Redox Couple in Suppressing Electron Conduction in Field-Effect Transistors. *Adv. Mater.* **2009**, *21*, 3087–3091.
71. Zahab, A.; Spina, L.; Poncharal, P.; Marlie, C.; Marlière, C. Water-Vapor Effect on the Electrical Conductivity of a Single-Walled Carbon Nanotube Mat. *Phys. Rev. B* **2000**, *62*, 10000.
72. Mudimela, P. R.; Grigoras, K.; Anoshkin, I. V.; Varpula, A.; Ermolov, V.; Anisimov, A. S.; Nasibulin, A. G.; Novikov, S.; Kauppinen, E. I. Single-Walled Carbon Nanotube Network

Field Effect Transistor as a Humidity Sensor. *J. Sensors* **2012**, *2012*, 1–7.
73. Na, P. S.; Kim, H.; So, H.-M.; Kong, K.-J.; Chang, H.; Ryu, B. H.; Choi, Y.; Lee, J.-O.; Kim, B.-K.; Kim, J.-J.; et al. Investigation of the Humidity Effect on the Electrical Properties of Single-Walled Carbon Nanotube Transistors. *Appl. Phys. Lett.* **2005**, *87*, 093101.
74. Pati, R.; Zhang, Y.; Nayak, S. K.; Ajayan, P. M. Effect of H_2O Adsorption on Electron Transport in a Carbon Nanotube. *Appl. Phys. Lett.* **2002**, *81*, 2638.

Supporting Information

Solution-Mediated Selective Nanosoldering of Carbon Nanotube Junctions for Improved Device Performance

Jae-Won Do,[1,2] Noel N. Chang,[3] David Estrada,[1,4,5] Feifei Lian,[1,4,6] Hyeongyun Cha,[7] Xiangyun J. Duan,[1] Richard T. Haasch,[8] Eric Pop,[1,2,4,6] Gregory S. Girolami,[2,3] Joseph W. Lyding[1,2*]

[1]*Department of Electrical and Computer Engineering, University of Illinois at Urbana-Champaign, Urbana, Illinois 61801, United States*
[2]*Beckman Institute for Advanced Science and Technology, University of Illinois at Urbana−Champaign, Urbana, Illinois 61801, United States*
[3]*Department of Chemistry, University of Illinois at Urbana-Champaign, Urbana, Illinois 61801, United States*
[4]*Micro and Nanotechnology Laboratory, University of Illinois at Urbana-Champaign, Urbana, Illinois 61801, United States*
[5]*Department of Materials Science and Engineering, Boise State University, Boise, Idaho, 83725, United States*
[6]*Department of Electrical Engineering, Stanford University, Stanford, California 94305, United States*
[7]*Department of Mechanical Science and Engineering, University of Illinois at Urbana-Champaign, Urbana, Illinois 61801, United States*
[8]*Frederick Seitz Materials Research Laboratory, University of Illinois at Urbana-Champaign, Urbana, Illinois 61801, United States*

[*]Corresponding author. E-mail: lyding@illinois.edu

Table of Contents:

1. Pd Precursor Study

a. Air Stability Test of CpPd(allyl) and $Pd_2(dba)_3$

In order to implement the solution-mediated and open-to-air process, we initially investigated the precursor, $C_5H_5PdC_3H_5$ (CpPd(allyl)), which is a volatile compound that undergoes thermal decomposition to deposit metallic Pd with the threshold temperature of about 250 °C without the use of a reducing co-reagent.[1] For the control study, the CpPd(allyl) precursor was dissolved in chloroform and spincoated onto a carbon nanotube (CNT) network device as a solution, which was allowed to evaporate in air. The device was exposed to vacuum for several hours where nanosoldering would normally take place, and the precursor was removed by washing with the same solvent thoroughly without actually performing the nanosoldering step; *i.e.* passing current through the CNT network. From this control study, a significant increase in the off currents of the CNT network devices was observed, leading to a large drop in the on/off current ratio. We believe this undesirable feature is a result of the air sensitivity of CpPd(allyl) precursor, which decomposes quickly once it is exposed to air and leaves randomly dispersed Pd deposits across the CNT network.

We then turned to another Pd precursor, $Pd_2(dba)_3$ (where dba = dibenzoylacetone), which is frequently used as a homogeneous catalyst in organic transformation for Pd source. We chose $Pd_2(dba)_3$ because it is soluble in common organic solvents such as chloroform, and it already contains zerovalent Pd metal center, making it ideal for spincoating application of the precursor on to different substrates in air.[2–4] We have performed the same control study as described above, and Figure S1 shows the changes in the on and off currents after CpPd(allyl) and $Pd_2(dba)_3$ precursors were spincoated on different CNT network devices and handled in air. As shown in Figure S1, the CpPd(allyl) precursor resulted in an increase in the off currents by an

average of ~1.72 × 10^{-9} A/μm, which is at least an order of magnitude higher than the initial off currents of the devices studied in our experiments. On the other hand, $Pd_2(dba)_3$ precursor did not result in any significant changes in both the on and off currents, indicating that the precursor does not result in any significant decomposition in air at least for the duration of two days during which the entire experiment took place and that any residue from the precursor does not add to the current transport in the CNT network.

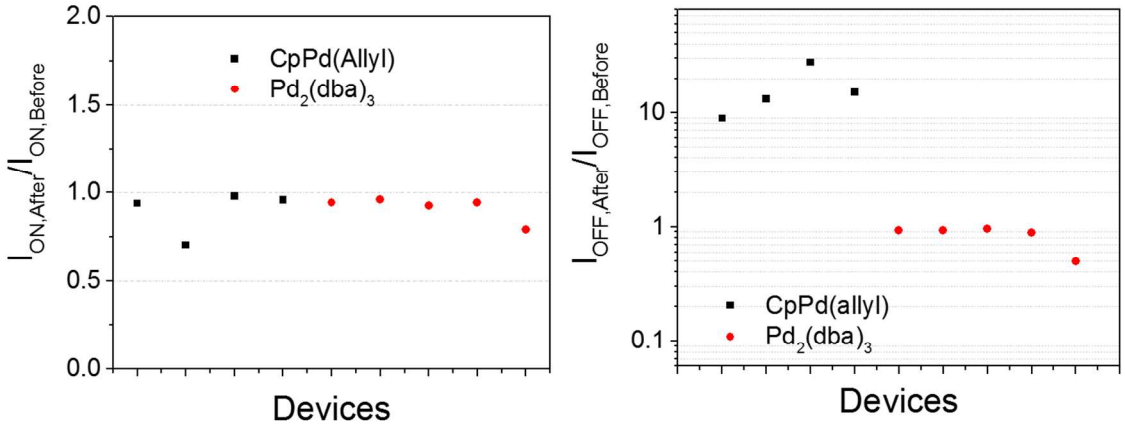

Figure S1. Summaries of changes in the on currents (left) and off currents (right) upon the control experiment with CpPd(allyl) precursor (black) and with $Pd_2(dba)_3$ precursor (red) without any current pass.

b. Thermogravimetric Analysis (TGA) and X-ray Photoelectron Spectroscopy (XPS), and Energy-Dispersive X-ray Spectroscopy (EDS) of $Pd_2(dba)_3$

In order to further investigate the thermal decomposition of $Pd_2(dba)_3$, we have performed thermogravimetric analysis (TGA). Figure S2 shows TGA of $Pd_2(dba)_3$, which was carried out under nitrogen environment with inset showing its molecular structure. TGA shows that the onset of mass loss for $Pd_2(dba)_3$ occurs at ~180 °C, followed by a gradual decrease until the mass plateaued at ~500 °C. The final mass of ~23% corresponds to the production of PdO or Pd(0) with some carbon contamination.

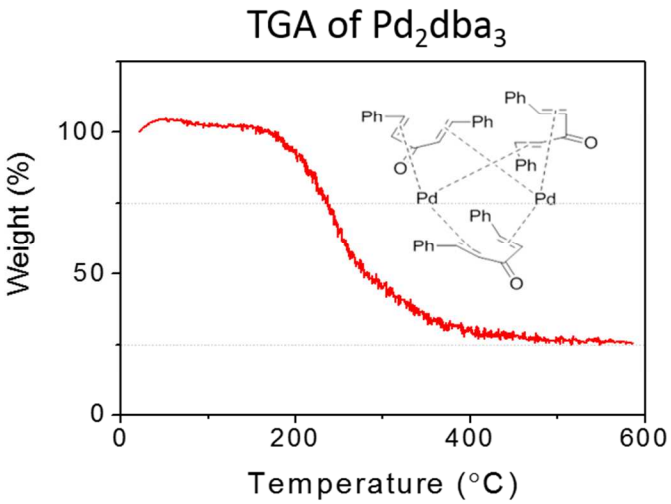

Figure S2. Thermogravietric analysis (TGA) and its molecular structure of $Pd_2(dba)_3$ as a precursor for Pd.

In order to further investigate the final deposits, *ex-situ* films were prepared by drop-casting ~10 μL of dichloromethane solution of $Pd_2(dba)_3$ (2 mM) on three separate silica substrates and evaporating the solvent in air. Each sample was then placed in a glass vial left either open to air (control and in air deposition) or sealed with a gas inlet connected to a vacuum manifold (vacuum deposition). The vials were heated to ~250 °C at 2.5 °C/min in a sand bath either at atmospheric pressure (air deposition) or at ~0.1 Torr (vacuum deposition), except for the control, which was stored at room temperature in atmosphere for the length of the experiment. After the samples cooled to room temperature, they were rinsed with dichloromethane to remove the byproducts and excess reactants, and dried in an air steam before the analyses using x-ray photoelectron spectroscopy (XPS) and energy-dispersive x-ray spectroscopy EDS (see Figures S3 and S4). XPS measurements were carried out with a Kratos Axis Ultra spectrometer using monochromatic aluminum Kα radiation using pass energies of 160 eV (survey spectra) and 40 eV (high-resolution spectra). EDS analysis was performed using a FEI XL-30 SEM with field emission gun (FEG) source.

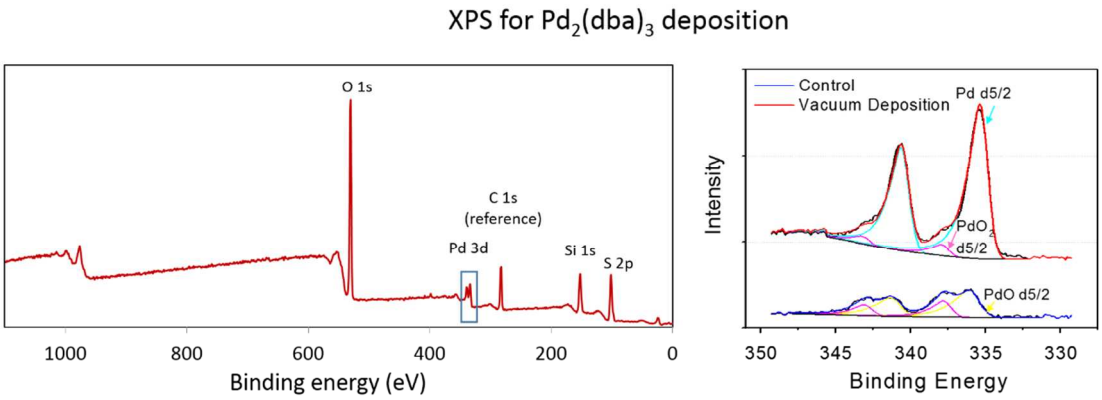

Figure S3. XPS survey (left) and high-resolution (right) spectra of silica substrates for $Pd_2(dba)_3$ study. Red curve corresponds to a sample where the deposited $Pd_2(dba)_3$ was heated under vacuum, followed by solvent rinsing, while blue curve corresponds to a control sample where the deposited $Pd_2(dba)_3$ was stored in air, followed by solvent rinsing.

As can be seen from XPS analysis in Figure S3, the control sample showed weak signals at binding energies that correspond to PdO and PdO_2, which are very likely present as impurities in the commercial reagent.[4] On the other hand, the sample that was heated in air exclusively contained PdO (data not shown), while the sample that was heated in vacuum contained predominantly metallic Pd. Figure S4 shows EDS spectra collected from the control and vacuum-heated samples under the same acquisition conditions. The EDS data indicate that the deposited material from the vacuum heating contains Pd, while the PdO and PdO_2 residues or impurities left on the control sample did not show any noticeable Pd peak, indicating that the amount of these residues are very little and below the detection limit of EDS. As also shown in the main text (Figure 2b), these residues or impurities also do not significantly affect the device performance.

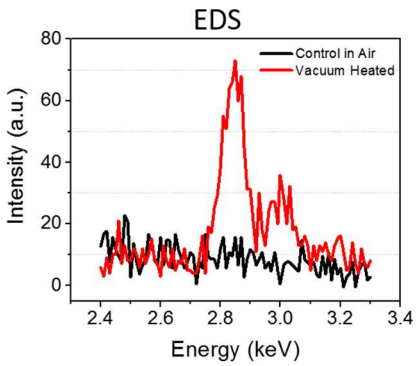

Figure S4. EDS spectra from the vacuum-heated sample (red) and the air-stored control sample (black).

2. Data Analysis and Control Experiments

All in-air and vacuum DC electrical characterizations in our experiments were performed with a Keithley 4200-SCS semiconductor analyzer and a Janis variable temperature probe station. As noted in the main text, transfer characteristics were measured in air for each device before metal deposition. After metal deposition and removal of the byproducts and excess precursor by rinsing the substrates with clean solvents, the transfer characteristics were measured again for comparison. We used threshold voltage (V_T) found by linear extrapolation method from peak conductance ($g_m = (dI_D/dV_{GS})_{max}$), I_{ON} at a constant V_{GS} overdrive from the forward sweep ($V_{GS} - V_{T,FWD}$ = -10 V), and I_{OFF} as the minimum I_{DS} from the same transfer curve to calculate the I_{ON}/I_{OFF} ratio. For devices with $V_{T,FWD}$ < -10 V, I_{DS} at V_{GS} = -15 V is used as I_{ON}, and the constant V_{GS} overdrive between V_{GS} = -15V and $V_{T,FWD}$ is used for both before and after metal deposition cases. This approach compares all devices at similar charge densities and reduces variability due to V_T shift, allowing a better comparison of performance across different devices. For devices with I_{OFF} lower than the measurement limit, the I_{OFF} was chosen by averaging currents in the regions with fluctuations in the off state below V_T.[5] We then compared the effect of our nanosoldering technique on the device field-effect mobility,[5] using $\mu_{FE} = g_m L/(WC_{OX}V_{DS})$ where C_{OX} = 1.04 × 10^{-8} F/cm^2 is the gate capacitance per unit area calculated from the parallel plate

model. The average and standard deviation of log on/off current ratio and mobility of our devices before Pd deposition are extracted as: 2.83 ± 0.64 and 2.15 ± 2.01 cm^2/V-s, respectively. We note that the parallel plate model highly overestimates the gate capacitance, thus underestimates μ_{FE} for low-density CNT networks because only a portion of the gate oxide is covered by CNT networks.[6–8] Image analysis with Gwyddion reveals that the fill factor of our networks is ~0.024; *i.e.* that approximately 2.4% of the device channel is covered by CNTs.[9]

For control experiments, CNT network devices were coated with $Pd_2(dba)_3$ using the similar conditions used for metal deposition; ~12.0 mg of $Pd_2(dba)_3$ was dissolved in 1.0 mL of chloroform, which was spincoated on to CNT network devices at 1500 rpm for 30 seconds, resulting in ~180 nm thick film of the precursor (see Figure S5a). After letting the chloroform evaporate in air, the CNT network devices were loaded into a vacuum chamber, and finally rinsed away without passing any current through the CNT network in order to test if any impurity or residue from the precursor could affect the device performance or if the precursor breaks down without heating under the given experimental conditions. Additional control experiments were conducted on different CNT network devices where devices were treated with similar Joule heating methods in vacuum but in the absence of the precursor, and then exposed back to air for sufficient time (over 24 hours) to test that the performance improvement was due to other experimental factors including current-induced annealing of contacts. Figures S5b and S5c summarize the degree of improvement in the I_{ON}/I_{OFF} ratio ($I_{ON}/I_{OFF,AFTER}$ / $I_{ON}/I_{OFF,BEFORE}$) and μ_{FE} ($\mu_{FE,AFTER}$ / $\mu_{FE,BEFORE}$) for these devices, along with the devices where Pd particles were deposited. As can be seen in the figure, the performance of control devices remained about the same, while the devices treated with Joule heating had an average improvements by factors of ~6.3 and ~6 in the I_{ON}/I_{OFF} and μ_{FE}, respectively.

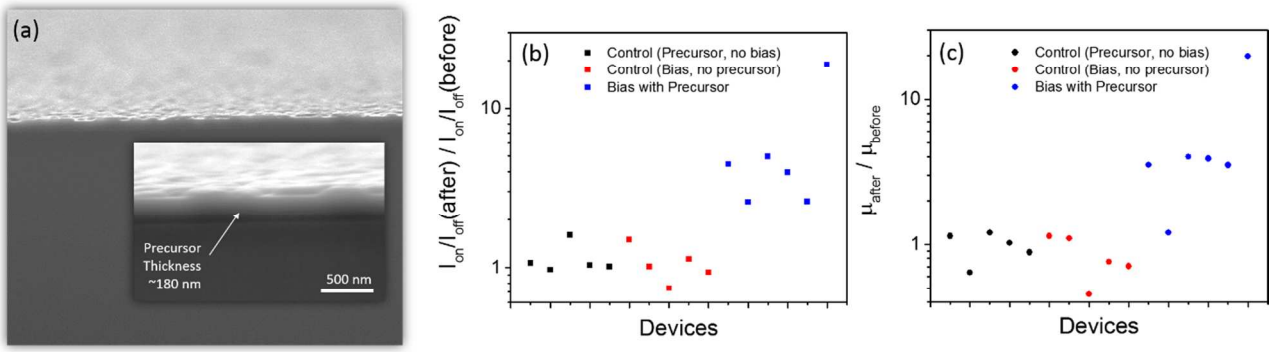

Figure S5. (a) Cross-section SEM image of spincoated $Pd_2(dba)_3$ film on silica substrate. (b, c) Summaries of improvement in I_{ON}/I_{OFF} ratios and μ_{FE} upon control experiment with precursor but no bias (black), with bias but no precursor (red), and upon Pd deposition with precursor and bias (blue).

3. Scanning Electron Microscope (SEM) and Atomic Force Microscope (AFM) Data

Figure S6a shows a CNT network device before spincoating the precursor and after depositing Pd and rinsing away the excess. Figure S6b, which shows a magnified SEM image of the area indicated by the red dotted box in Figure S6a, clearly indicates that Pd was selectively deposited at the CNT junctions; *i.e.* at hot spots under device operation. The inset in Figure S6b shows an atomic force microscope (AFM) image of the area indicated by the blue box. The height profiles from the AFM image show that some of the larger Pd nanoparticles are ~100 – 130 nm in height (Figures S6c and S6d), whereas others, which were not noticeable in the SEM images, are sub-60 nm in height (Figures S6e and S6f). In addition to the selectively deposited Pd particles, small particles of ~15 nm in height are randomly scattered over the SiO_2 surface (Figure S6g), which we attribute to impurities present in the spincoating solution. Figure S6h shows a typical height profile for our CVD-grown CNTs, whose average diameter is 2.4 ± 1.1 nm as judged from AFM analysis.

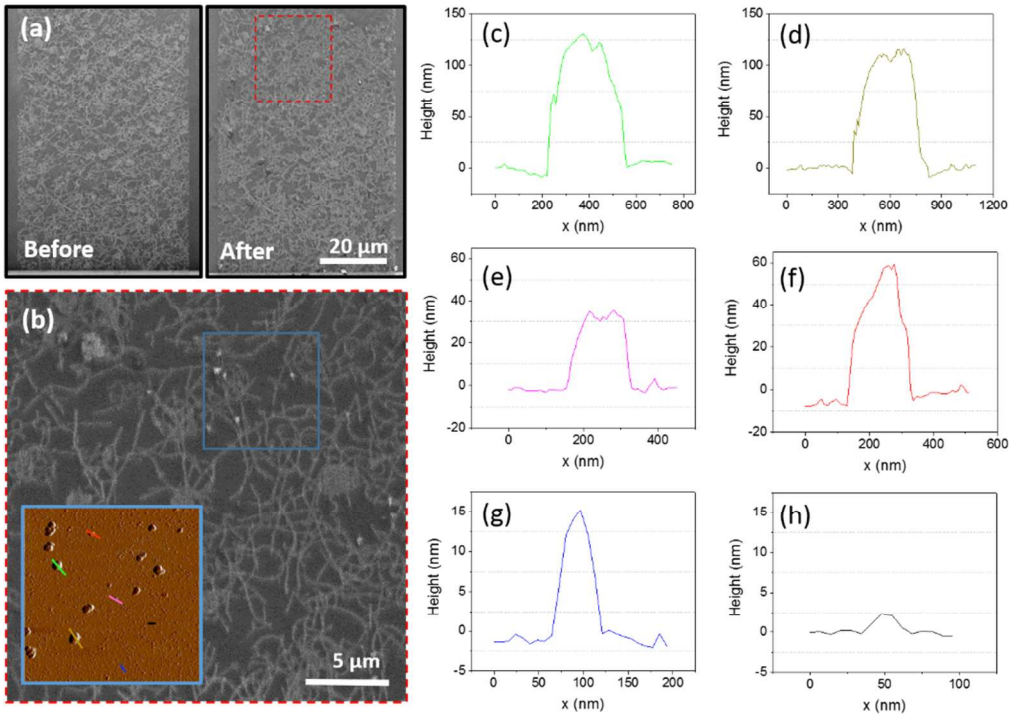

Figure S6. (a) SEM images of a CNT network (left) before and (right) after Pd deposition. **(b)** Zoomed-in SEM image of CNT network indicated by red dotted box in (a) with inset showing AFM image of the region indicated by the blue box. The dimensions of AFM image are 7 µm × 7 µm. **(c-d)** Height profiles of large deposited Pd particles along the green and dark yellow lines in the AFM image of (b). **(e-f)** Height profiles of smaller deposited Pd particles along the pink and red lines. **(g)** Height profile of even smaller particle that is typically found randomly scattered over the surface. **(h)** Height profile of a typical CNT grown by CVD.

References

(1) Hierso, J.-C.; Serp, P.; Feurer, R.; Kalck, P. MOCVD of Rhodium, Palladium and Platinum Complexes on Fluidized Divided Substrates: Novel Process for One-Step Preparation of Noble-Metal Catalysts. *Appl. Organomet. Chem.* **1998**, *12*, 161–172.

(2) Old, D. W.; Wolfe, J. P.; Buchwald, S. L. A Highly Active Catalyst for Palladium-Catalyzed Cross-Coupling Reactions: Room-Temperature Suzuki Couplings and Amination of Unactivated Aryl Chlorides. *J. Am. Chem. Soc.* **1998**, *120*, 9722–9723.

(3) Sumida, Y.; Kato, T.; Yoshida, S.; Hosoya, T. Palladium-Catalyzed Regio- and Stereoselective Hydrosilylation of Electron-Deficient Alkynes. *Org. Lett.* **2012**, *14*, 1552–1555.

(4) Zalesskiy, S. S.; Ananikov, V. P. $Pd_2(dba)_3$ as a Precursor of Soluble Metal Complexes and Nanoparticles: Determination of Palladium Active Species for Catalysis and Synthesis. *Organometallics* **2012**, *31*, 2302–2309.

(5) Timmermans, M. Y.; Estrada, D.; Nasibulin, A. G.; Wood, J. D.; Behnam, A.; Sun, D.; Ohno, Y.; Lyding, J. W.; Hassanien, A.; Pop, E.; *et al.* Effect of Carbon Nanotube Network Morphology on Thin Film Transistor Performance. *Nano Res.* **2012**, *5*, 307–319.

(6) Cao, Q.; Kim, H.; Pimparkar, N.; Kulkarni, J. P.; Wang, C.; Shim, M.; Roy, K.; Alam, M. A.; Rogers, J. A. Medium-Scale Carbon Nanotube Thin-Film Integrated Circuits on Flexible Plastic Substrates. *Nature* **2008**, *454*, 495–500.

(7) Cao, Q.; Xia, M.; Kocabas, C.; Shim, M.; Rogers, J. A.; Rotkin, S. V. Gate Capacitance Coupling of Singled-Walled Carbon Nanotube Thin-Film Transistors. *Appl. Phys. Lett.* **2007**, *90*, 023516.

(8) Wang, C.; Chien, J.-C.; Takei, K.; Takahashi, T.; Nah, J.; Niknejad, A. M.; Javey, A. Extremely Bendable, High-Performance Integrated Circuits Using Semiconducting Carbon Nanotube Networks for Digital, Analog, and Radio-Frequency Applications. *Nano Lett.* **2012**, *12*, 1527–1533.

(9) Estrada, D.; Pop, E. Imaging Dissipation and Hot Spots in Carbon Nanotube Network Transistors. *Appl. Phys. Lett.* **2011**, *98*, 073102.